ROYAL SOCIETY
OF CHEMISTRY

PAPER

Check for updates

Tailoring capping-layer composition for improved stability of mixed-halide perovskites†

Noor Titan Putri Hartono, [ID] *[ai] Marie-Hélène Tremblay, [ID] [b] Sarah Wieghold,[c] Benjia Dou, [ID] [a] Janak Thapa,[a] Armi Tiihonen, [ID] [a] Vladimir Bulovic,[a] Lea Nienhaus, [ID] [d] Seth R. Marder,*[befgh] Tonio Buonassisi*[a] and Shijing Sun [ID] *[aj]

Incorporating a low dimensional (LD) perovskite capping layer on top of a perovskite absorber, improves the stability of perovskite solar cells (PSCs). However, in the case of mixed-halide perovskites, which can undergo halide segregation into single-halide perovskites, a systematic study of the capping layer's effect on mixed-halide perovskite absorber is still lacking. This study bridges this gap by investigating how the 1D perovskite capping layers on top of $MAPb(I_xBr_{1-x})_3$ ($x = 0, 0.25, 0.5, 0.75, 1$) absorbers affect the films' stability. We utilize a new method, dissimilarity matrix, to investigate the image-based stability performance of capping-absorber pair compositions across time. This method overcomes the challenge of analyzing various film colors due to bandgap difference in mixed-halide perovskites. We also discover that the intrinsic absorber stability plays an important role in the overall stability outcome, despite the capping layer's support. Within the 55 unique capping-absorber pairs, we observe a notable 1D perovskite material, 1-methoxynaphthalene-2-ethylammonium chloride (2MeO–NEA–Cl or 9-Cl), that improves the stability of $MAPbI_3$ and $MAPb(I_{0.5}Br_{0.5})_3$ by at least 8 and 1.5 times, respectively, compared to bare films under elevated humidity and temperature. Surface photovoltage results also show that the accumulation of electrostatic charges on the film surface depends on the capping layer type, which could contribute to the acceleration/deceleration of degradation.

Introduction

To push perovskite solar cells (PSCs) towards the manufacturing stage, the lack of stability of hybrid organic–inorganic perovskite (HOIP) materials remains a significant challenge. In recent years, single-junction PSCs have benefited from incorporating a thin low-dimensional (LD) perovskite layer

on top of their perovskite absorbers, which are referred to as heterostructure/capping layer. Examples of A-site cation introduced to form LD perovskites are phenylethylammonium (PEA)[1] and octylammonium (OA).[2] The LD perovskite capping layer is formed by reacting the excess PbI_2 within the absorber with a spin coated, low-concentration organic halide salt solution. This strategy improves the environmental stability,[3] and in some cases also boosts efficiency due to improved surface passivation.[2]

Most PSC studies have been focused on lead–iodide perovskites for single-junction solar cells. However, perovskite tandem cells require a wide-bandgap perovskite film as a top cell, mainly absorbing between 1.7–1.9 eV.[4] A well-established approach to increase the bandgap is by mixing the iodine with bromine in the HOIP, for instance, shifting the bandgap from 1.6 eV for methylammonium lead iodide ($MAPbI_3$) to about 1.87 eV for 50% : 50% methylammonium lead iodide–bromide ($MAPb(I_{0.5}Br_{0.5})_3$).[5] Similar to single-junction PSCs, perovskite-based tandem cells have also explored the 2D perovskite capping layer strategy mainly for improving surface passivation, and therefore, device performance,[6,7] as opposed to exploring the impact on stability.[8] However, systematic studies on how to best select capping layer for improving the stability of I–Br-mixed absorbers are still lacking. Additionally, the vast

[a]*Massachusetts Institute of Technology, 77 Massachusetts Avenue, Cambridge, MA 02139, USA. E-mail: nhartono@mit.edu; noortitan@alum.mit.edu; buonassisi@mit.edu; shijings@mit.edu*

[b]*Georgia Institute of Technology, North Avenue, Atlanta, GA 30332, USA*

[c]*Argonne National Laboratory, 9700 S. Cass Avenue, Lemont, IL 60439, USA*

[d]*Florida State University, Department of Chemistry and Biochemistry, 95 Chieftan Way, Tallahassee, FL 32306, USA*

[e]*University of Colorado Boulder, Renewable and Sustainable Energy Institute, Boulder, CO 80303, USA. E-mail: Seth.Marder@colorado.edu*

[f]*University of Colorado Boulder, Department of Chemical and Biological Engineering, Boulder, CO 80303, USA*

[g]*University of Colorado Boulder, Department of Chemistry, Boulder, CO 80303, USA*

[h]*National Renewable Energy Laboratory, Chemistry and Nanoscience Center, Golden, CO 80401, USA*

[i]*Helmholtz-Zentrum Berlin für Materialien und Energie GmbH, Kekuléstraße 5, 12489 Berlin, Germany*

[j]*Toyota Research Institute, Los Altos, CA, 94022, USA*

† Electronic supplementary information (ESI) available. See DOI: 10.1039/d1ta07870d

This journal is © The Royal Society of Chemistry 2022

J. Mater. Chem. A, 2022, **10**, 2957–2965 | **2957**

number of organic A-site cation candidates also warrants a high-throughput screening method to be conducted.

Therefore, in this study we explore how the systematic change in halide ratio of the absorber, coupled with various previously unexplored 1D perovskites as the capping layer, affects its environmental stability. To do this, we select cations that are known to favor the formation of 1D perovskite rather than 2D.[9] We screen these absorber-capping pairs under elevated temperature (85 °C) and relative humidity ((80 ± 2)% RH). We utilize advanced data analysis methods for extracting the image data from the aging test, to find the most stable capping layer composition quickly, for a given absorber composition. We also improve the feature importance rank output by including sub-structure-related descriptors, such as the functional groups in the capping layer materials. The surface photovoltage (SPV) of absorber-capping pairs is also measured to understand the electrostatic properties upon varying the absorber or capping layer composition. Our approach advances the screening process for finding the most stable capping layer materials which will benefit the wide-bandgap perovskite solar cells field.

Result and discussion

Study overview and objectives

We consider 10 different 1D perovskites as capping layers, and the mixture of MAPbI$_3$ and MAPbBr$_3$ for widening the bandgap. The films are then degraded in an in-house aging test chamber, with (80 ± 2)% RH, 85 °C, and 0.16 sun illumination. The film color change is captured by automatically photographing the samples in every 3 minutes. This image data is processed, where the red, green, blue (RGB) values for each image is extracted using the protocol that has been published previously.[3,10] The large dataset is subsequently analyzed using dissimilarity matrix to extract the most stable capping layer material for each absorber composition. Using this method, we can also compare the samples variance within the same composition and across different compositions. The extensive list of benefits for using this method will be elaborated shortly.

No single capping layer material improves all the absorbers investigated in this study; this highlights the complexity of designing capping layer for the mixed-halide HOIP. The stable capping layer depends on the composition of the perovskite absorber beneath it. Therefore, the optimal capping-absorber pairs need to be further characterized to understand their optoelectronic and structural properties at the film-level. Based on the use of multiple characterization techniques and data analysis, we created a shortlist of the capping-absorber pairs with high stability that are promising to be incorporated in device-level. The overview of the study is shown in Fig. 1.

Capping-absorber pair compositions and degradation data extraction

The 1D perovskite precursors consist of 10 phenyl- and naphthalene-based A-site cations with chlorine and bromine as the anions, along with a state-of-art stable capping layer

material, phenyltriethylammonium iodide (PTEAI), that tends to form quasi-2D perovskites with the underlying perovskite absorber.[3] We use the PTEAI as the benchmark to the 1D capping performance. These 1D perovskite precursors have not been explored previously, and they have similar molecular structures. With the exception of the PTEAI, all the A-site cations have a primary amine/methyl group, as shown in Fig. 1a. In addition, other functional groups include: nitrile (C≡N) in 1-Cl (2CN–PEA–Cl), ester (R–CO$_2$–R′) in 2-Cl (2-CO$_2$Me–PEA–Cl) and 7-Cl (3CO$_2$Me–PEA–Cl), ether (R–O–R′) in 9-Cl (2MeO–NEA–Cl) and 10-I (2MeO–PMA–I), and nitro (R–NO$_2$) in 4-I (2NO$_2$–PEA–I) and 5-Cl (3NO$_2$–PEA–Cl); where PEA is phenethylammonium, NEA is naphthylethylammonium, and PMA is phenylmethylammonium.

We tested the capping layer stability performance for each of the absorber layer materials consisting of various 25%-increment MAPb(I$_x$Br$_{1-x}$)$_3$. The bare absorber layers show increasing bandgap due to incorporation of higher Br compositions, indicated by the change in film color, shown in Fig. 1a. With the combinations of 11 different capping layer materials including PTEAI and the 5 different absorber compositions, the total samples fabricated are 407, including the repeated samples.

The next steps in the process of image data analysis are shown in Fig. 1b. As the films degrade under exposure to environmental stress, the film colors change over time. Based on the film images which are captured every 3 minutes, the average RGB values at each time point for the whole area of the film is extracted. The RGB values of each sample are further analyzed using dissimilarity matrices to extract a single value metric and compared across different sample degradations.

Dissimilarity matrix for screening capping-absorber pairs

Since the total number of samples is more than 400, it is challenging to analyze the trend across different capping-absorber pairs, due to various films' starting, final, and transition colors in between. In the case of 100% MAPbI$_3$ absorber the color change is easier to observe because the dark films turn to yellow color due to MAPbI$_3$ degrading into PbI$_2$.[3] However, the addition of MAPbBr$_3$ into the absorber in 25%-increment changes the degradation pathways (e.g. halide segregation in addition to the PbI$_2$ formation), and thus, the color of the films as they degrade. An added complication is the requirement for a method for comparing the 4-dimensional data: RGB values, and time for different samples.

A dissimilarity matrix is suitable for looking at the overview of a large, multi-dimensional dataset. The m by m matrix shows how dissimilar/similar the samples are, where each row and column represents a specific sample with their own data vector. Each (a,b) matrix cell contains a value that represents how dissimilar/similar the vector of sample a and sample b is, by calculating the distance between the two vectors.

Some commonly used distance measures for similarity analysis are Minkowski (e.g. Manhattan, Euclidean), L1, inner product (e.g. Jaccard, cosine), squared chord, and squared L2.[11] One of the distance measures, cosine similarity, has been widely implemented for various purposes, including face

2958 | J. Mater. Chem. A, 2022, **10**, 2957–2965

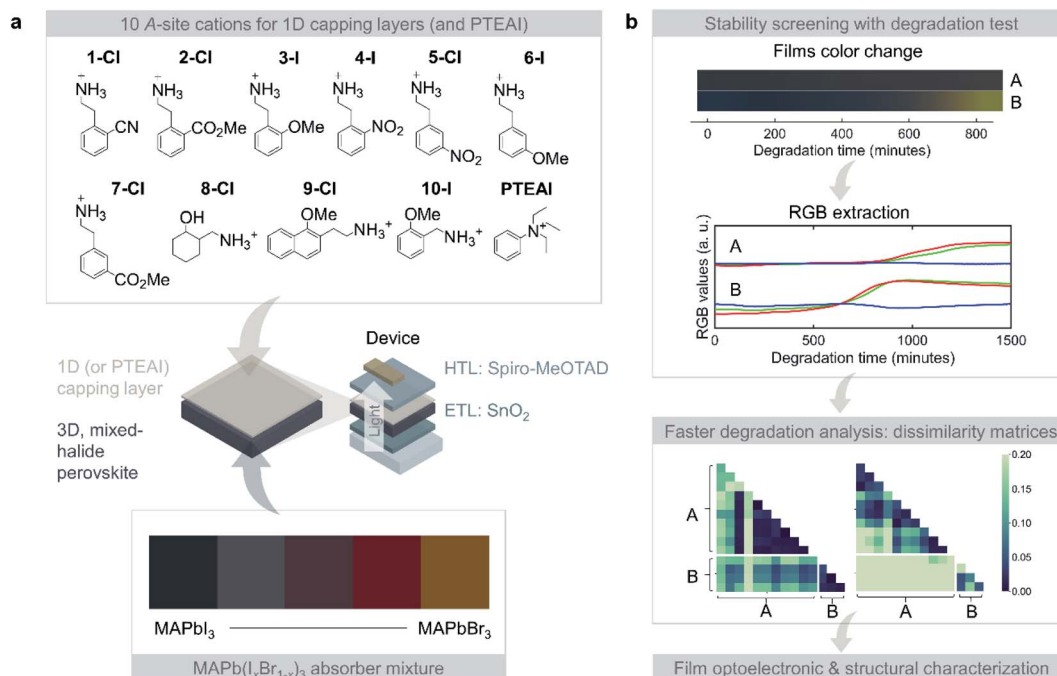This journal is © The Royal Society of Chemistry 2022

Fig. 1 The capping-absorber compositions and degradation film color analysis during degradation. (a) A-site cations of 1D perovskite materials and PTEAI for capping layer and the 3D mixed-halide perovskite composition of $MAPb(I_xBr_{1-x})_3$. The capping layer materials are the following: 1-Cl (2CN–PEA–Cl), 2-Cl (2-CO$_2$Me–PEA–Cl), 3-I (2MeO–PEA–I), 4-I (2NO$_2$–PEAI), 5-Cl (3NO$_2$–PEA–Cl), 6-I (3MeO–PEA–I), 7-Cl (3CO$_2$Me–PEA–Cl), 8-Cl (2HO–CycMA–Cl), 9-Cl (2MeO–NEA–Cl), 10-I (2MeO–PMA–I), and PTEAI (phenyltriethylammonium iodide). (b). The films color change during aging test is used to extract the red, green, blue (RGB) values, and is further used for the dissimilarity matrix analysis. Then, the optoelectronic and structural characterizations are analyzed for the capping-absorber pair of interest.

verification,[12,13] text classification,[14] and automated essay scoring.[15] The robustness of the cosine distance measure is evident from its wide-use across different fields, for evaluating the similarity between datasets, by calculating the L2-normalized dot product of vectors. The larger distance between 2 vectors is, the higher the dissimilarity matrix value is.

In this study, dissimilarity matrices with cosine distance are used to evaluate the aforementioned 4-dimensional degradation data consisting of RGB values and time, to compare the sample set. The 4-dimensional data is collapsed into a single dissimilarity value, which is the distance between the 2 vectors, making it faster and easier to find the pattern in the data. The dissimilarity matrix is constructed using pairwise distance algorithm from scikit-learn.[16]

A hypothetical example of dissimilarity matrix is shown in ESI Fig. S1.† If we have 3 materials and 2 of them have 2 samples, we will have a 5 by 5 dissimilarity matrix. When the dissimilarity value is high in the color bar, the samples are dissimilar, and vice versa. It should be noted that the variance of samples is also observed from the dissimilarity matrix. When repeated samples have low variance, the dissimilarity values among the samples will be low.

In this study, we consider the RGB values from 0–999 minutes. Under the aging testing conditions, the samples with poor stability have fully degraded by 999 minutes, while the ones with superior stability maintain the initial color. The RGB values from time point 0 to 999 minutes are then appended to form a vector for one sample. The vectors, are thus calculated to

form the dissimilarity matrix, which thus reflects the color change during the period of interest.

According to our data analysis, we identify two promising capping layers which resulted in an extended film stability compared to all other compositions studied here and are chosen for further analysis. The results of the dissimilarity matrix analysis are shown in Fig. 2a for the two chosen capping layers: PTEAI and 9-Cl. The 9-Cl capping layer extends the bare film stability by at least 8 and 1.5 times, respectively, for $MAPbI_3$ and $MAPb(I_{0.5}Br_{0.5})_3$ absorber, while PTEAI capping layer extends the bare film stability by ~3 times for $MAPb(I_{0.75}Br_{0.25})_3$ absorber. The degradation results for the two capping layers are shown in Fig. 2b, while the results for other capping layer materials are shown in ESI Fig. S2.† Note that the dissimilarity matrix only shows the samples' similarities/dissimilarities, and does not show if one sample is better/worse than the others. Therefore, after narrowing down to specific samples of interest, it is important to check the color changes, shown in Fig. 2b. The dissimilarity matrix results across the other metrics, Manhattan and Euclidean distance measures, are consistent with the cosine distance measure, as shown in ESI Fig. S3.†

Based on the dissimilarity matrix result, we recorded the following observations: (1) bare $MAPbI_3$ film samples have high variance in comparison to the Br-mixed samples (see Fig. 2c and d), indicated by the bare $MAPbI_3$ samples' higher dissimilarity value; (2) both PTEAI and 9-Cl capping layers are effective in reducing the dissimilarity value among samples within the same absorber composition that indicates a reduction in

This journal is © The Royal Society of Chemistry 2022

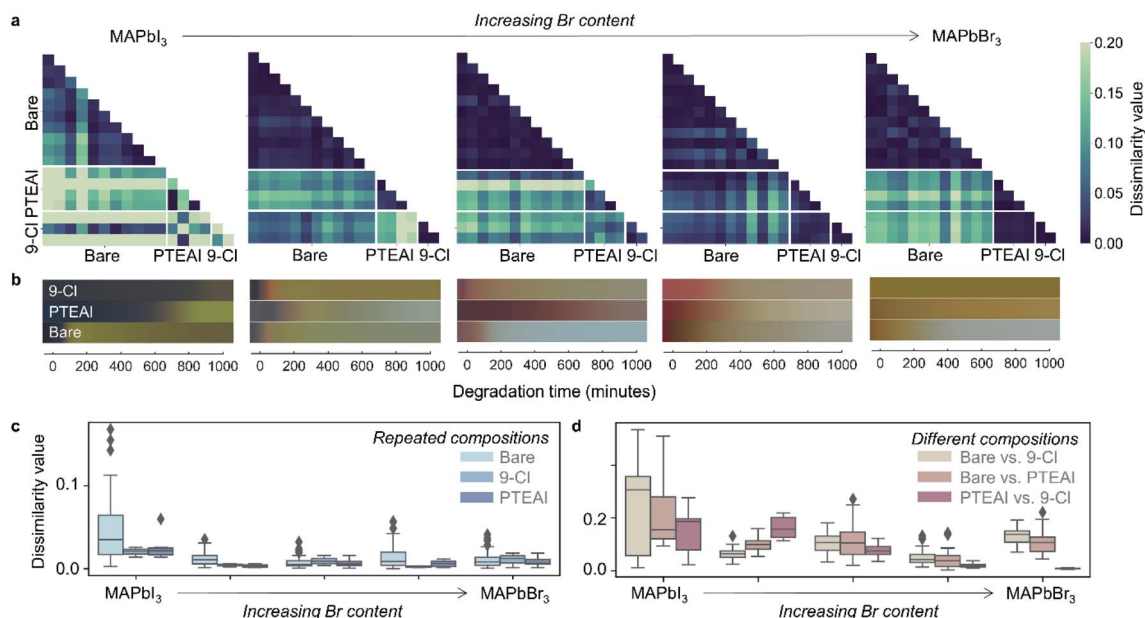J. Mater. Chem. A, 2022, 10, 2957–2965 | 2959

Fig. 2 The dissimilarity matrix of degradation films' color change over time. (a) The dissimilarity matrices (for $t = 999$ minutes) using cosine distance measure, (b) the degradation film color change of bare, PTEAI-capped, and 9-Cl-capped mixed-halide absorber (MAPb(I_xBr_{1-x})$_3$) films during degradation, and the boxplot summary of dissimilarity values for (c) repeated compositions and (d) different compositions.

samples variability, especially in MAPbI$_3$, by 44% (PTEAI) and 57% (9-Cl), as shown in Fig. 2c, which is important in manufacturing and scaling-up; (3) the degradation of PTEAI-capped and 9-Cl-capped MAPb($I_{0.75}Br_{0.25}$)$_3$ absorber is the most distinct in comparison to each other (Fig. 2d), which shows that for this specific absorber, using PTEAI as the capping layer leads to a better stability than 9-Cl; (4) the stability of both PTEAI and 9-Cl capping layers are similar in high-Br absorbers. These observations highlight the complexity of degradation paths of HOIP which is discussed more extensively in the ESI.†

Intrinsic absorber stability and degradation mechanisms

We can also use instability index,[17] which uses integrated RGB color change over the aging test duration to evaluate how stable the films are. However, note that the instability index only observes the total color change, but does not consider how the shape of RGB curves changes over time. The instability index results for bare, PTEAI-capped, and 9-Cl-capped films are shown in Fig. 3a. In the case of mixed-halide absorbers, which suffer from photoinduced segregation, capping layers have limited power in suppressing the degradation. On the other hand, the 9-Cl-capped MAPbBr$_3$ film shows a significant improvement in degradation, in comparison to the mixed-halide absorbers.

We can determine the most important features in contributing to the film stability by analyzing the Shapley values[18] from the degradation data. We use the degradation test dataset consisting of 407 samples to train a random forest regression model following an established protocol[3] for cross-validation, train-test dataset split, and data pre-processing using python-based scikit-learn library.[16] 27 features are included as the input, including some features from previously published

study,[3] such as the molecular properties of the capping layers, and the processing conditions of the capping layer. There are two types of features in this analysis, the 0D descriptors, which have no molecular shape information, and the 1D descriptors, which are related to certain substructures but not bond lengths,[19] as shown in Fig. 3b. The 0D features are related to the absorber (MAPbBr$_3$ amount), processing conditions (concentration and annealing temperature of the capping layer precursor solution), number of certain atoms, and molecular properties (molecular weight, number of rotatable bonds, topological polar surface area, partition coefficient, and topological index). The 1D features are the functional groups present in the A-site cations (nitro, nitrile, phenyl, naphthyl, ester, ether, alcohol, primary or quaternary amine), as shown in Fig. 3c. Most of these features are calculated from ChemDraw and ChemOffice software package. The 1D descriptors include the functional groups, because most of the A-site cations have similar functional groups. The output of the random forest regression model for this dataset is the instability index defined earlier in this work.

1D descriptors of molecules, especially when used for feature importance rank, can provide a guidance on selecting the specific shape of molecules to achieve high stability, as supposed to general properties such as number of certain atoms or molecular weights. Ideally, overcoming limitations in incorporating higher dimensional descriptors, 2D (*e.g.* molecular graph representations involving bonds between atoms) and 3D (*e.g.* distances between certain atomic pairs in the molecule),[19] will provide a more accurate molecular representation and improve the interpretability of the results.

The Shapley values analysis in Fig. 3d shows that one of the 1D features, the presence of ester functional group, such as in 2-
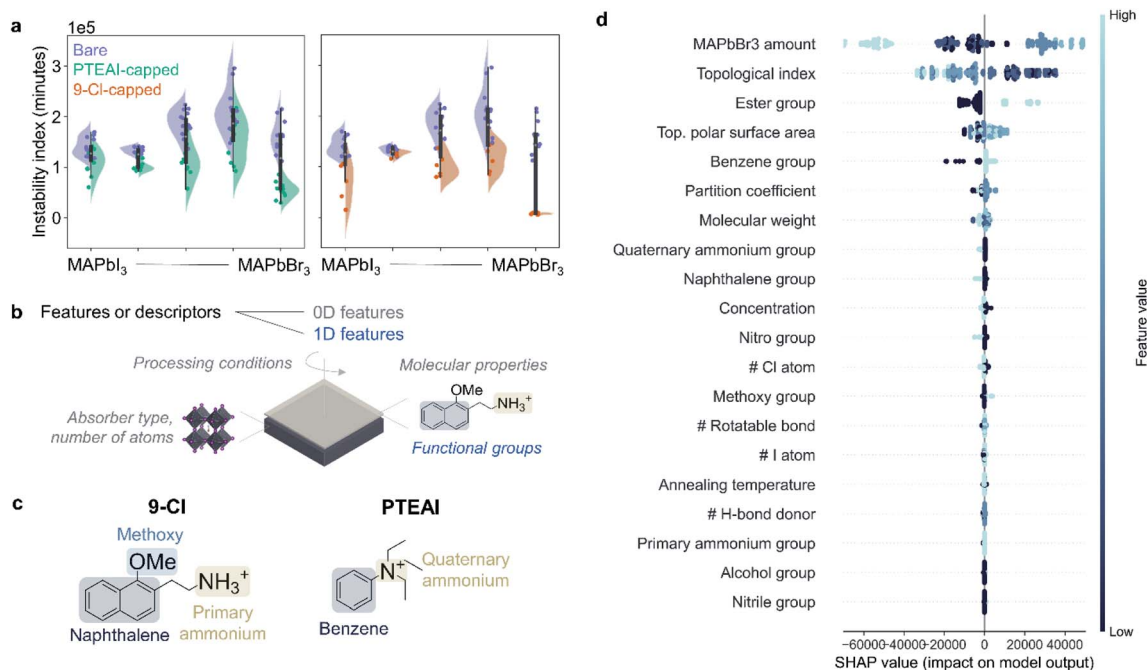
2960 | *J. Mater. Chem. A*, 2022, **10**, 2957–2965

This journal is © The Royal Society of Chemistry 2022

Fig. 3 Feature importance rank based on improved descriptors. (a) The instability index results for bare, PTEAI-capped, and 9-Cl-capped films across absorber compositions. (b) Two types of descriptors, 0D (processing conditions, absorber type, number of atoms, molecular properties) and 1D (functional groups). (c) Examples of capping layer materials broken down by their functional groups, which are included as features. (d) Top 20 features affecting the degradation of capping-absorber pairs, sorted from the most important to least important. High SHAP value indicates high instability index.

Cl and 7-Cl, decreases the stability, and this descriptor ranks the third. Although a small amount of different type of ester-based molecule, L-ascorbic acid, has previously been shown to improve the formamidinium (FA)-based perovskite phase stability by forming multiple hydrogen bonds with FA + ions,[20] a further investigation on why the ester-based capping layer materials are unstable in mixed-halide absorber is needed.

The second descriptor that affects instability index the most is the topological index, which indicates the A-site cation's complexity in the capping layer. The increase in topological index of capping layer leads to a more stable thin film.

The top rank in Shapley values analysis result shows that the amount of Br$^-$ in the absorber contributes to the instability of the films, which exceeds the effect coming from the capping layer material itself, and how it is deposited. This suggests that the intrinsic instability of the mixed-halide perovskite absorber, MAPb(I$_x$Br$_{1-x}$)$_3$, can only be alleviated moderately by the LD perovskites in the capping layer. This is due to light-induced halide phase segregation in mixed-halide system, leading to I-rich and Br-rich domains.[21,22] Several possible explanations to this phenomenon have been investigated, such as intrinsically metastable mixed-halide alloys,[23] polaron formation that leads to local strain,[24,25] positive free energies of mixing,[26–28] electrons trapped by defect states and holes trapped in I-rich domains causing electric fields that drive demixing,[29] trapped carrier concentration gradient leading to strain or thermalization energy,[30] and surface defect carrier trapping leading to electric field-induced anion drift.[31,32]

Therefore, as confirmed by both the instability index and Shapley value analysis result, the optimum capping layer for stable perovskite film significantly depends on the absorber composition. Additional characterization is therefore needed to identify the degradation mechanisms for the materials of interest and investigate why the stability improvement due to the capping layer is limited in mixed-halide absorbers.

Optical, crystal structure, and surface electric potential

It is important to know whether the capping layer alters the bandgap and absorptance of the film especially if the capping layer is implemented for perovskite–perovskite tandem cells. The films with newly identified capping layer material of interest, 9-Cl, is assessed with UV-Vis absorption measurements. PTEAI capping layer also performs well, but its properties have been previously investigated.[3] The absorptance result for 9-Cl capped films is shown in Fig. 4a. The absorptance lines with deeper color are the 9-Cl-capped films, while the ones with lighter color are the bare films. Comparing the non-capped with 9-Cl-capped film, the absorptance of MAPb(I$_x$Br$_{1-x}$)$_3$ with $x = 1$, 0.25, and 0 has no observable difference, indicating that the bandgap for 9-Cl-capped film atop of these absorbers is unaltered. However, in the case of $x = 0.75$, and 0.5, the bandgap of 9-Cl-capped films is blue-shifted.

The powder x-ray diffraction (PXRD), as shown in Fig. 4b, reveals the film structure. As more I$^-$ is replaced by Br$^-$ in MAPb(I$_x$Br$_{1-x}$)$_3$ (x decreases), the PXRD peak shifts from 14.12° for MAPbI$_3$ to 14.96° for MAPbBr$_3$, due to smaller ionic radius of

This journal is © The Royal Society of Chemistry 2022

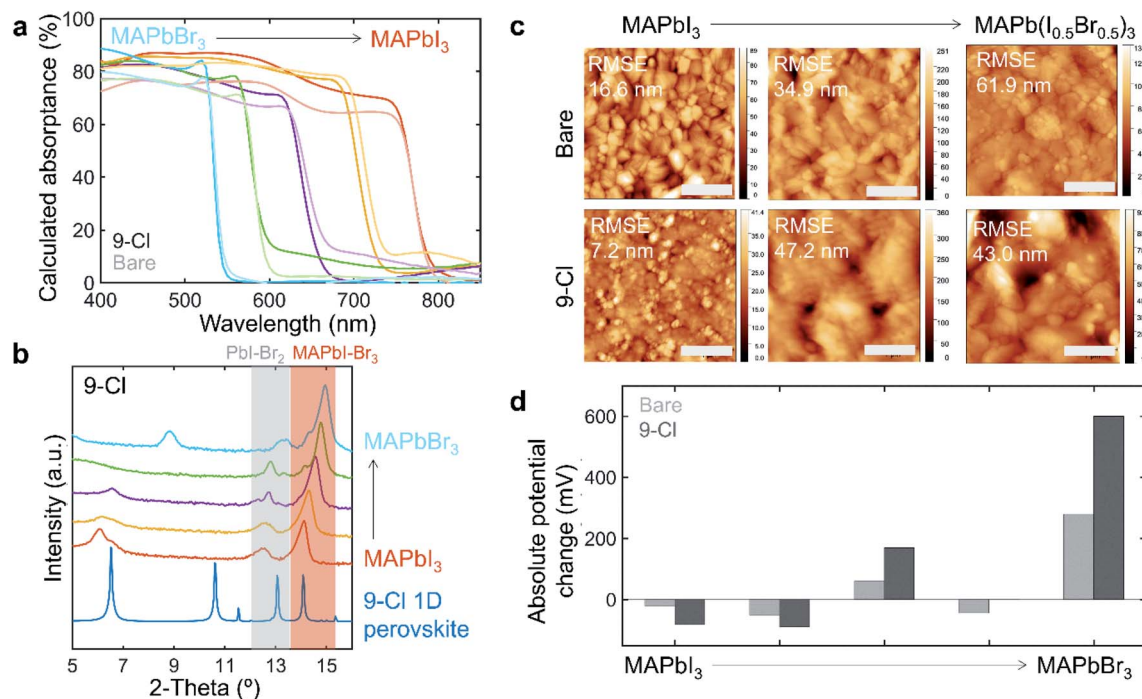*J. Mater. Chem. A*, 2022, **10**, 2957–2965 | **2961**

Fig. 4 The optoelectronic, crystal structure, and surface passivation properties of 9-Cl capping layer. (a) The absorptance of the 9-Cl capped in comparison to bare films. (b) The crystal structure for the 9-Cl-capped $MAPb(I_xBr_{1-x})_3$ perovskite films in comparison to the 9-Cl 1D perovskite PXRD result. (c) The surface morphology of 9-Cl-capped films in comparison to bare films measured using AFM with scale bar of 1 μm. (d) The absolute potential change result based on surface photovoltage measurement for bare and 9-Cl-capped $MAPb(I_xBr_{1-x})_3$ perovskite films.

Br^- than I^-. Similar to the $MAPb(I–Br)_3$ peak shift, the $Pb(I–Br)_2$ peak also shifts from 12.44° to 13.4°. The low-dimensional perovskite peaks in the capping layer appear at low 2θ-angles. Depending on the absorber composition, the low-dimensional perovskite peaks appear at different angles, indicating that the I–Br ratio plays an important role in forming the type of low-dimensional perovskite structure within the capping layer. We also observe that the low 2θ-angle peak also appears less crystalline in the mixed-halide absorber, as shown in ESI Fig. S5,† indicating that the capping layer is more amorphous, which could potentially lead to a less protection for the absorber underneath. This could also be due to the addition of Br in the lattice, although it is harder to conclude, due to the shift in low 2θ-angle peaks position as we shift towards $MAPbBr_3$.

Atomic force microscopy (AFM) shows the morphology of the film surface and the surface roughness, as shown in Fig. 4c. In both 9-Cl-capped $MAPbI_3$ and $MAPb(I_{0.5}Br_{0.5})_3$ films, the surface roughness and its variation are greatly reduced. However, that is not the case for 9-Cl-capped $MAPb(I_{0.75}Br_{0.25})_3$ film. In case of $MAPb(I_xBr_{1-x})_3$, the bromine addition into the perovskite film generally increases the surface roughness, which could be due to formation of aggregate crystals.[33]

The device performance for 9-Cl-capped and bare $MAPb(I_xBr_{1-x})_3$ for $x = 1$ and 0.75 is also measured. The result is shown in ESI Fig. S6.† The efficiency of the 9-Cl-capped device is reduced due to lower short-circuit current (J_{SC}) in the case of $x = 1$ even though the open-circuit voltage (V_{OC}) is maintained. In the case of $x = 0.75$, the efficiency ends up to be higher, because

of improvement in V_{OC}. We also measured the recombination dynamics of the capped-films using time-resolved photoluminescence (TRPL) and found that depositing capping layer on the absorber might actually introduce surface defects, as shown in ESI Fig. S7.† This shows that the improvement in stability could not compensate the loss in efficiency. We should also note that the device performance still requires several optimization rounds, which might lead to a better performance.

To understand how the illumination-induced surface potential changes as the capping layer is introduced, surface photovoltage (SPV) measurements are conducted. Fig. 4d shows the summary of SPV results showing the absolute potential change between dark and white light-illuminated measurements for bare and 9-Cl-capped $MAPb(I_xBr_{1-x})_3$ films. The I-rich absorbers show negative potential change, indicating p-type material, while the Br-rich absorbers show positive potential change, indicating n-type material. In comparison to the bare films, introducing 9-Cl capping layer enhances the absolute potential change effect.

Conclusion

This study systematically investigates the effect of the mixed-halide absorber compositions with 1D capping layers on the films' environmental stability. Ten 1D perovskites were introduced for the first time and were compared with the state-of-the-art 2D capping material, PTEAI. They are used to synthesize 55 unique capping-absorber pairs, which are degraded under high humidity and high temperature. We utilize

dissimilarity matrices for observing the high-dimensional data coming from the films' color change. This method helps in comparing samples within and across compositions and leads to the discovery of 2MeO–NEA–Cl (9-Cl) as an excellent capping layer for improving the stability of MAPbI$_3$ and MAPb(I$_{0.5}$Br$_{0.5}$)$_3$. We find that the capping layer changes the potential on the film's surface differently depending on the absorber composition, by enhancing p-type and n-type characteristics for I-rich and Br-rich absorbers, respectively, which might be one of the reasons for composition-dependent degradation results. We discover that capping layers have a limited power in improving those mixed-halide absorbers that are intrinsically unstable. We perform several material characterizations, including surface photovoltage, which probes the surface net electrostatic charge of the films. Our study advances the wide-bandgap perovskite solar cells field by introducing advanced methods for screening the stability of capping-mixed halide perovskite absorber pairs in the film, and discovering a new stable 1D capping layer material.

Methods

1D perovskite ammonium bromide/chloride powder synthesis

Cations and 1D perovskite crystal were synthesized as previously reported.[34] In general, PbI$_2$ (1 eq.) was added in HI (57 weight% aqueous solution) and stirred at 130 °C for until fully dissolved. A solution of the salt of the R(NH$_2$)$_n$NH$_3^+$ cation (2 eq.) in HI (or HI and MeOH) was added and the resultant mixture was stirred at 130 °C for 2 min. The solution was then allowed to crystallize at room temperature for 24 h. The solids were filtered and dried under high vacuum.

Film and capping layer fabrication

For 3-D methylammonium lead iodide (MAPbI$_3$) precursor solution: 1.5 M PbI$_2$ (TCI chemicals) solution was dissolved in 9 : 1 DMF : DMSO mixed solvents, before mixing them with ammonium powder. For every gram of methylammonium iodide (MAI) powder (Dyenamo), we added 5.10 mL PbI$_2$ stock solution correspondingly, which corresponds to MAI : PbI$_2$ molar ratio of 1 : 1.09. The same protocol was followed for making methylammonium lead bromide (MAPbBr$_3$) precursor solution. The mixed-halide perovskite precursor solutions were made by mixing MAPbI$_3$ and MAPbBr$_3$ precursor solutions in 3 : 1, 1 : 1, and 1 : 3 ratios.

Capping layer solutions were made in 10 mM concentration, by mixing previously synthesized ammonium bromide/ammonium chloride powder with isopropyl alcohol, pure, ACS reagent, ≥99.5% (Sigma-Aldrich).

65 μL of MAPbI$_3$ solution was then deposited on the pre-cleaned substrate (glass slides for UV-Vis and XRD, ITO substrates for AFM and KPFM), and spin coated with this 2-step recipe: 1000 rpm for 10 seconds and acceleration of 200 rpm s^{-1}, then 6000 rpm for 30 seconds and acceleration of 2000 rpm s^{-1}. 5 seconds after the start of the second step, 150 μL of chlorobenzene was dropped on the substrate. Then, the deposited film was annealed on the hotplate at 100 °C for 10 minutes. After the substrate is cooled down, 60 μL of capping layer solution was deposited on top, and spin coated with 3000 rpm speed for 30 seconds. The substrate was then annealed at 100 °C for 10 minutes.

Device fabrication

ITO substrates are cleaned as follows: ultrasonic bath in acetone and isopropanol for about 10 min respectively; UV–ozone treatment for 20 min. SnO$_2$ nanoparticle solution is diluted with DI water to 3% (wt/wt) with 3 mg mL^{-1} KCl as the additive. The resulting solution is spin coat at 3000 rpm for 30 s with acceleration of 3000 rpm s^{-1} and annealed at 150 °C for 30 min. Perovskite films and the capping layers are prepared as previous session. Spiro-MeOTAD solution contains 72 mg spiro-MeOTAD, 1 mL chlorobenzene, 17.5 μL Li-TFSI stock solution (520 mg mL^{-1} Li-TFSI in acetonitrile) and 28.8 μL t-BP. The solution is then spin-coated at 4000 rpm (4000 rpm s^{-1} acceleration) for 30 s on the perovskite. Finally, a 70 nm for Au is thermally evaporated on the spiro-MeOTAD to finish the device.

General characterization

The crystal structure and the film phases were characterized using X-ray diffraction (XRD, Rigaku SmartLab), with Cu-Kα sources. Samples were stored in inert conditions inside a nitrogen-purged glovebox between synthesis and aging test/characterization steps. The film's absorptances were measured using UV-Vis spectrophotometer (PerkinElmer Lambda 950) between 350–1000 nm. The AFM and KPFM measurements were performed using a Veeco Multimode 8 (Bruker). The topography images were measured in ScanAsyst mode using a silicon cantilever. For the KPFM experiments, a Ti/Pt cantilever was used and a voltage of 3 V was applied to the cantilever to measure the surface contact potential difference. For the SPV analysis, a white light source from the top was employed. PL decay lifetimes were measured via time-correlated single photon counting (TCSPC) under 405 nm excitation (LDH-D-C-405, PicoQuant) at an average power of 3.2 mW. To collect the photon arrival times, a HydraHarp 400 (PicoQuant) and a single-photon avalanche photodiode (Micro Photon Devices) were used. A 550 nm LP filter was used to remove excess laser scatter. J–V characteristics of the devices were measured in ambient environment with a Keithley 2400 source meter under AM1.5 100 mW cm^{-2} irradiance. The light source is calibrated with encapsulated Si cell certified by the National Renewable Energy Laboratories (NREL). The device areas are 0.15 cm^2, defined by a metal mask. The J–V curves were measured from 1.3 V to −0.2 V and then backwards.

Accelerated aging chamber and image acquisition

The films were degraded in an environmentally-controlled chamber under (80 ± 2)% RH, 85 °C, and 0.16 sun illumination. A camera was taking a picture every 3 minutes during the aging process, and the images (in PNG format) were calibrated following an established protocol,[3,17] and the red, green, blue (RGB) values over time for each sample.

This journal is © The Royal Society of Chemistry 2022

J. Mater. Chem. A, 2022, 10, 2957–2965 | 2963

Data integrity

The project data was generated in different forms. The film fabrication conditions are collected in a laboratory notebook, while the image data generated were stored in the cloud service (Dropbox). Raw materials characterization data were processed using either MATLAB or Python.

Dissimilarity matrix analysis

The dissimilarity matrix utilizes the pairwise distance metric available at scikit-learn.[16] The distance metric is a function $d(a,b)$ such that $d(a,b) < d(a,b)$ if objects a and b are more similar than objects a and c. In this study, we use the cosine similarity metric, that computes the L2-normalized dot product of the vectors, as shown in eqn (1).[11,16]

$$d(x,y) = 1 - \frac{\sum_{i=1}^{n} x_i y_i}{\sqrt{\sum_{i=1}^{n} x_i^2} \sqrt{\sum_{i=1}^{n} y_i^2}} \tag{1}$$

In addition, the Euclidean metric is the non-normalized L2 dot product of the vector difference, as shown in eqn (2).[11,16] The Euclidean-based dissimilarity matrix analysis is shown in ESI Fig. S3.†

$$d(x,y) = \sqrt{\sum_{i=1}^{n} |x_i - y_i|^2} \tag{2}$$

Data availability

The dissimilarity matrix analysis code and experimental data are available in GitHub repository (https://github.com/PV-Lab/dissimatrix). The pairwise distance algorithm is implemented using scikit-learn.[16]

Author contributions

M. H. T. synthesized the 1D perovskite capping layers. N. T. P. H., S. W., B. D., J. T., L. N., and L. N. fabricated samples (films and devices), performed aging test, performed materials characterizations, and measured device performances. N. T. P. H., S. W., L. N., and S. S. interpreted experimental results. V. B., S. R. M., S. S., and T. B. supervised the study. N. T. P. H., S. S., and T. B. contributed to the writing the paper. All the authors discussed the implications of the work and edited the paper.

Conflict of interests

Although our laboratory has IP filed covering photovoltaic technologies and materials informatics broadly, we do not envision a direct COI with this study, for which code & data are open sourced. One of the authors (T. B.) own equity in a startup company applying machine learning to materials.

Acknowledgements

References

1 P. Chen, Y. Bai, S. Wang, M. Lyu, J.-H. Yun and L. Wang, *Adv. Funct. Mater.*, 2018, **28**(17), 1706923.

2 J. J. Yoo, S. Wieghold, M. C. Sponseller, M. R. Chua, S. N. Bertram, N. T. P. Hartono, J. S. Tresback, E. C. Hansen, J.-P. Correa-Baena, V. Bulović, T. Buonassisi, S. S. Shin and M. G. Bawendi, *Energy Environ. Sci.*, 2019, **12**, 2192–2199.

3 N. T. P. Hartono, J. Thapa, A. Tiihonen, F. Oviedo, C. Batali, J. J. Yoo, Z. Liu, R. Li, D. F. Marrón, M. G. Bawendi, T. Buonassisi and S. Sun, *Nat. Commun.*, 2020, **11**, 1–9.

4 M. Jošt, L. Kegelmann, L. Korte and S. Albrecht, *Adv. Energy Mater.*, 2020, **10**, 1904102.

5 G. Longo, C. Momblona, M. G. La-Placa, L. Gil-Escrig, M. Sessolo and H. J. Bolink, *ACS Energy Lett.*, 2018, **3**, 214–219.

6 S. Gharibzadeh, B. Abdollahi Nejand, M. Jakoby, T. Abzieher, D. Hauschild, S. Moghadamzadeh, J. Schwenzer, P. Brenner, R. Schmager, A. Haghighirad, L. Weinhardt, U. Lemmer, B. Richards, I. Howard and U. Paetzold, *Adv. Energy Mater.*, 2019, **9**(21), 1803699.

7 S. Gharibzadeh, I. M. Hossain, P. Fassl, B. A. Nejand, T. Abzieher, M. Schultes, E. Ahlswede, P. Jackson, M. Powalla, S. Schäfer, M. Rienäcker, T. Wietler, R. Peibst, U. Lemmer, B. S. Richards and U. W. Paetzold, *Adv. Funct. Mater.*, 2020, **30**, 1909919.

8 T. Duong, H. Pham, T. C. Kho, P. Phang, K. C. Fong, D. Yan, Y. Yin, J. Peng, M. A. Mahmud, S. Gharibzadeh, B. A. Nejand, I. M. Hossain, M. R. Khan, N. Mozaffari, Y. Wu, H. Shen, J. Zheng, H. Mai, W. Liang, C. Samundsett, M. Stocks, K. McIntosh, G. G. Andersson, U. Lemmer, B. S. Richards, U. W. Paetzold, A. Ho-Ballie, Y. Liu, D. Macdonald, A. Blakers, J. Wong-Leung, T. White, K. Weber and K. Catchpole, *Adv. Energy Mater.*, 2020, **10**, 1903553.

9 A. H. Proppe, M. H. Tremblay, Y. Zhang, Z. Yang, R. Quintero-Bermudez, S. O. Kelley, S. Barlow, S. R. Marder and E. H. Sargent, *J. Phys. Chem. C*, 2020, **124**, 24379–24390.

2964 | *J. Mater. Chem. A*, 2022, **10**, 2957–2965

This journal is © The Royal Society of Chemistry 2022

10 S. Sun, A. Tiihonen, F. Oviedo, Z. Liu, J. Thapa, Y. Zhao, N. T. P. Hartono, A. Goyal, T. Heumueller, C. Batali, A. Encinas, J. J. Yoo, R. Li, Z. Ren, I. M. Peters, C. J. Brabec, M. G. Bawendi, V. Stevanovic, J. Fisher and T. Buonassisi, A Physical Data Fusion Approach to Optimize Compositional Stability of Halide Perovskites, *Matter*, 2021, **4**(4), 1305–1322.

11 H. A. Abu Alfeilat, A. B. A. Hassanat, O. Lasassmeh, A. S. Tarawneh, M. B. Alhasanat, H. S. Eyal Salman and V. B. S. Prasath, Effects of Distance Measure Choice on K-Nearest Neighbor Classifier Performance: A Review, *Big Data*, 2019, **7**, 221–248.

12 H. V. Nguyen and L. Bai, in *Lecture Notes in Computer Science (Including Subseries Lecture Notes in Artificial Intelligence and Lecture Notes in Bioinformatics)*, Springer LNCS, Berlin, Heidelberg, 2011, vol. 6493, pp. 709–720.

13 P. Xia, L. Zhang and F. Li, *Inf. sci.*, 2015, **307**, 39–52.

14 B. Li and L. Han, in *Lecture Notes in Computer Science (Including Subseries Lecture Notes in Artificial Intelligence and Lecture Notes in Bioinformatics)*, Springer LNCS, Berlin, Heidelberg, 2013, vol. 8206, pp. 611–618.

15 A. R. Lahitani, A. E. Permanasari and N. A. Setiawan, in *Proceedings of 2016 4th International Conference on Cyber and IT Service Management, CITSM 2016*, Institute of Electrical and Electronics Engineers Inc., 2016.

16 F. Pedregosa, G. Varoquaux, A. Gramfort, V. Michel, B. Thirion, O. Grisel, M. Blondel, P. Prettenhofer, R. Weiss, V. Dubourg, J. Vanderplas, A. Passos, D. Cournapeau, M. Brucher, M. Perrot and É. Duchesnay, *J. Mach. Learn. Res.*, 2011, **12**, 2825–2830.

17 S. Sun, A. Tiihonen, F. Oviedo, Z. Liu, J. Thapa, Y. Zhao, N. T. P. Hartono, A. Goyal, T. Heumueller, C. Batali, A. Encinas, J. J. Yoo, R. Li, Z. Ren, I. M. Peters, C. J. Brabec, M. G. Bawendi, V. Stevanovic, J. Fisher and T. Buonassisi, *Matter*, 2021, **4**, 1305–1322.

18 S. M. Lundberg and S.-I. Lee, in *31st Conference on Neural Information Processing Systems*, 2017, pp. 4765–4774.

19 A. Tiihonen, S. J. Cox-Vazquez, Q. Liang, M. Ragab, Z. Ren, N. T. P. Hartono, Z. Liu, S. Sun, C. Zhou, N. C. Incandela, J. Limwongyut, A. S. Moreland, S. Jayavelu, G. C. Bazan and T. Buonassisi, *J. Am. Chem. Soc.*, 2021, **143**, 18917–18931.

20 X. Feng, M. Tan, M. Li, H. Wei and B. Yang, *Nano Lett.*, 2021, **21**, 1500–1507.

21 M. C. Brennan, S. Draguta, P. V. Kamat and M. Kuno, *ACS Energy Lett.*, 2018, **3**, 204–213.

22 M. C. Brennan, A. Ruth, P. V. Kamat and M. Kuno, *Trends Chem.*, 2020, **2**, 282–301.

23 F. Brivio, C. Caetano and A. Walsh, *J. Phys. Chem. Lett.*, 2016, **7**, 1083–1087.

24 C. G. Bischak, A. B. Wong, E. Lin, D. T. Limmer, P. Yang and N. S. Ginsberg, *J. Phys. Chem. Lett.*, 2018, **9**, 3998–4005.

25 C. G. Bischak, C. L. Hetherington, H. Wu, S. Aloni, D. F. Ogletree, D. T. Limmer and N. S. Ginsberg, *Nano Lett.*, 2017, **17**, 1028–1033.

26 S. Draguta, O. Sharia, S. J. Yoon, M. C. Brennan, Y. V. Morozov, J. M. Manser, P. V. Kamat, W. F. Schneider and M. Kuno, *Nat. Commun.*, 2017, **8**, 1–8.

27 X. Wang, Y. Ling, X. Lian, Y. Xin, K. B. Dhungana, F. Perez-Orive, J. Knox, Z. Chen, Y. Zhou, D. Beery, K. Hanson, J. Shi, S. Lin and H. Gao, *Nat. Commun.*, 2019, **10**, 1–7.

28 A. Ruth, M. C. Brennan, S. Draguta, Y. V. Morozov, M. Zhukovskyi, B. Janko, P. Zapol and M. Kuno, *ACS Energy Lett.*, 2018, **3**, 2321–2328.

29 A. J. Knight, A. D. Wright, J. B. Patel, D. P. McMeekin, H. J. Snaith, M. B. Johnston and L. M. Herz, *ACS Energy Lett.*, 2019, **4**, 75–84.

30 A. J. Barker, A. Sadhanala, F. Deschler, M. Gandini, S. P. Senanayak, P. M. Pearce, E. Mosconi, A. J. Pearson, Y. Wu, A. R. Srimath Kandada, T. Leijtens, F. De Angelis, S. E. Dutton, A. Petrozza and R. H. Friend, *ACS Energy Lett.*, 2017, **2**, 1416–1424.

31 R. A. Belisle, K. A. Bush, L. Bertoluzzi, A. Gold-Parker, M. F. Toney and M. D. McGehee, *ACS Energy Lett.*, 2018, **3**, 2694–2700.

32 E. T. Hoke, D. J. Slotcavage, E. R. Dohner, A. R. Bowring, H. I. Karunadasa and M. D. McGehee, *Chem. Sci.*, 2015, **6**, 613–617.

33 L. Atourki, E. Vega, B. Marí, M. Mollar, H. Ait Ahsaine, K. Bouabid and A. Ihlal, *Appl. Surf. Sci.*, 2016, **371**, 112–117.

34 M.-H. Tremblay, PhD thesis, Georgia Institute of Technology, 2020.

This journal is © The Royal Society of Chemistry 2022

J. Mater. Chem. A, 2022, **10**, 2957–2965 | **2965**